

Lightweight self-conjugate nucleus ^{80}Zr

A. Hamaker^{1,2,3*}, E. Leistenschneider^{1,2,†}, R. Jain^{1,2,3}, G. Bollen^{1,2,3}, S.A. Giuliani^{1,4,5}, K. Lund^{1,2}, W. Nazarewicz^{1,3}, L. Neufcourt¹, C. Nicoloff^{1,2,3}, D. Puentes^{1,2,3}, R. Ringle^{1,2}, C.S. Sumithrarachchi^{1,2}, I.T. Yandow^{1,2,3}

¹Facility for Rare Isotope Beams, Michigan State University, East Lansing, Michigan 48824, USA. ²National Superconducting Cyclotron Laboratory, Michigan State University, East Lansing, Michigan 48824, USA. ³Department of Physics and Astronomy, Michigan State University, East Lansing, Michigan 48824, USA. ⁴European Centre for Theoretical Studies in Nuclear Physics and Related Areas (ECT*-FBK), Trento, Italy. ⁵Department of Physics, Faculty of Engineering and Physical Sciences, University of Surrey, Guildford, Surrey GU2 7XH, United Kingdom. *Corresponding author: hamaker@nsl.msu.edu

[†]Current address: CERN, Geneva, Switzerland.

Protons and neutrons in the atomic nucleus move in shells analogous to the electronic shell structures of atoms. Nuclear shell structure varies across the nuclear landscape due to changes of the nuclear mean field with the number of neutrons N and protons Z . These variations can be probed with mass differences. The $N=Z=40$ self-conjugate nucleus ^{80}Zr is of particular interest as its proton and neutron shell structures are expected to be very similar, and its ground state is highly deformed. In this work, we provide evidence for the existence of a deformed double shell closure in ^{80}Zr through high precision Penning trap mass measurements of $^{80-83}\text{Zr}$. Our new mass values show that ^{80}Zr is significantly lighter, and thus more bound than previously determined. This can be attributed to the deformed shell closure at $N=Z=40$ and the large Wigner energy. Our statistical Bayesian model mixing analysis employing several global nuclear mass models demonstrates difficulties with reproducing the observed mass anomaly using current theory.

Understanding the mechanisms of structural evolution, especially for exotic nuclei far from the beta stability line, is a major challenge in nuclear science^{1,2}. In this context, a rich territory for studies of basic nuclear concepts is the neutron-deficient region around mass number $A = 80^3$. The nuclei in this region rapidly change their properties with proton and neutron numbers. Indeed, some of these nuclei are among the most deformed in the nuclear chart and exhibit collective behaviour, while others show non-collective excitation patterns characteristic of spherical systems.

The appearance of strongly deformed configurations around ^{80}Zr has been attributed to the population of the intruder $g_{9/2}$ orbitals separated by the spherical $N = Z = 40$ subshell closure from the upper- pf shell. This particular shell structure results in coexisting configurations of different shapes predicted by theory⁴⁻⁹. In particular, for the nucleus ^{80}Zr , spherical and deformed (prolate, oblate, and triaxial) structures are expected to coexist at low energies, and their competition strongly depends on the size of the calculated spherical $N = Z = 40$ gap¹⁰. Experimentally, ^{80}Zr has a very large prolate quadrupole deformation $\beta_2 \approx 0.4^{11,12}$. Within

the mean-field theory, this has been attributed to the appearance of the large deformed gap at $N = Z = 40$ in the deformed single-particle spectrum⁵. Consequently, the nucleus ^{80}Zr can be viewed as a deformed doubly-magic system.

In addition to shape-coexistence effects, ^{80}Zr is a great laboratory for isospin physics. Having equal number of protons and neutrons, this nucleus is self-conjugate; hence, it offers a unique venue to study proton-neutron pairing, isospin breaking effects, and the Wigner energy reflecting an additional binding in self-conjugate nuclei and their neighbours^{13,14}.

The mass of an isotope is a sensitive indicator of the underlying shell structure as it reflects the net energy content of a nucleus, including the binding energy. Hence, doubly-magic nuclei are significantly lighter, or more bound, compared to their neighbours. Due to a lack of precision mass measurement data on ^{80}Zr and its neighbours, it is difficult to characterize the size of the shell effect responsible for the large deformation of ^{80}Zr . To this end, we performed high precision Penning trap mass spectrometry of four neutron-deficient zirconium isotopes – $^{80-83}\text{Zr}$ – and analysed the local trends of the binding-energy surface by studying several binding-energy indicators. To quantify our findings, experimental patterns have been interpreted using global nuclear mass models augmented by a Bayesian model averaging analysis¹⁵.

Experimental Procedure

$^{80-83}\text{Zr}$ are highly neutron-deficient unstable radioisotopes of zirconium with half-lives ranging between 4.6 s and 42 s¹⁷, so they must be produced in specialized facilities and probed using fast and sensitive instrumentation. A schematic of the experimental setup and procedure is shown in Figure 1. The Zr isotopes were produced at the National Superconducting Cyclotron Laboratory’s Coupled Cyclotron Facility via projectile fragmentation of a 140 MeV/u ^{92}Mo primary beam that was impinged on a thin Be target. The produced Zr nuclei were separated from other fragments by the A1900 Fragment Separator¹⁸ and sent to the Advanced Cryogenic Gas Stopper¹⁹, where they were stopped as ions. The ions were extracted from the gas stopper as a low energy (30 keV/Q) continuous beam and selected by their mass-to-charge ratio (A/Q) using a dipole magnet. The

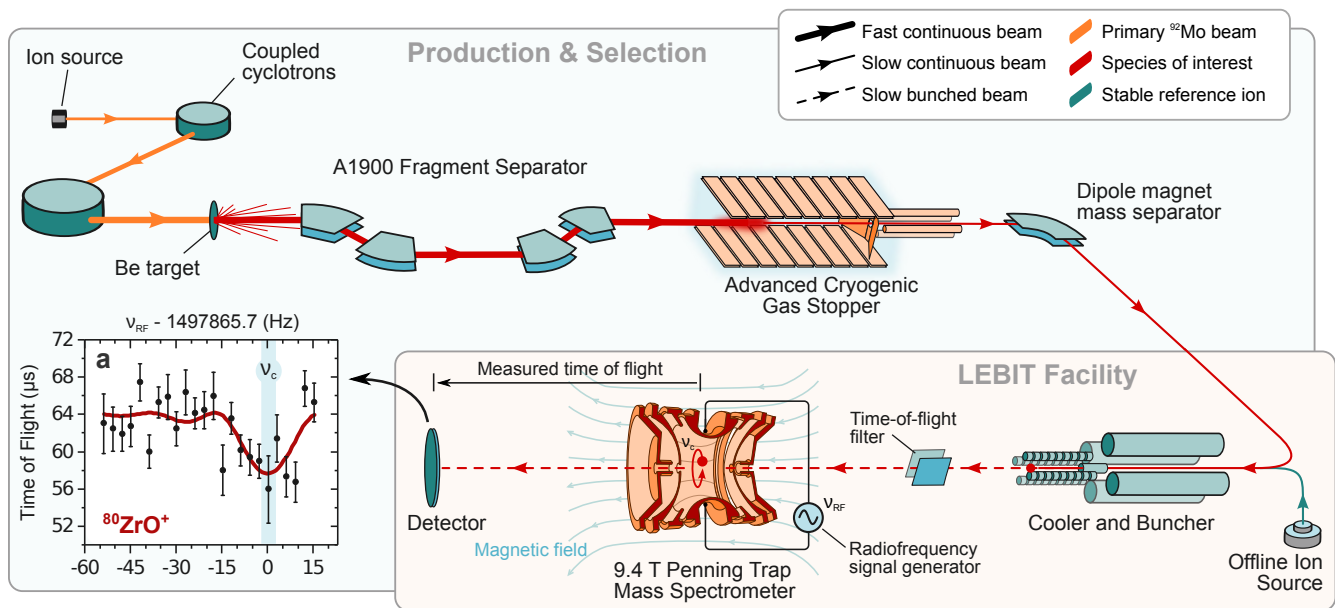


Figure 1. **The experimental procedure.** The relevant components of the experimental setup are displayed. Panel **a** shows a sample time-of-flight spectrum of a $^{80}\text{Zr}^{16}\text{O}^+$ molecular ion. The red curve is an analytical fit to the data¹⁶. The error bars represent the statistical uncertainty of the time-of-flight measurement, and the light blue band shows the 1σ uncertainty of the cyclotron frequency determination. See the main text and Methods for details.

ions were then sent to the Low Energy Beam and Ion Trap (LEBIT) facility²⁰. $^{80,82}\text{Zr}$ ions were sent as singly charged oxides ($A/Q = 96, 98$ respectively); $^{81,83}\text{Zr}$ ions were sent bare and doubly charged ($A/Q = 40.5, 41.5$ respectively).

Upon entering the LEBIT facility, the ions first passed through the cooler and buncher²¹ where they were accumulated, cooled, and released as short bunches to the LEBIT 9.4 T Penning trap²². A series of purification techniques described in Methods were employed to ensure nearly pure samples of the ion of interest were used for the measurement. A schematic of the LEBIT setup is shown in Fig. 1.

In the Penning trap, the mass m_{ion} of an ion with charge q was determined by measuring the cyclotron frequency $\nu_c = qB/(2\pi m_{\text{ion}})$ of the ion's motion about the trap's magnetic field, which has a strength B . The cyclotron frequency ν_c was measured using the time-of-flight ion cyclotron resonance (TOF-ICR) technique¹⁶, illustrated in Fig. 1 and described in Methods. The theoretical line shapes¹⁶ for the TOF-ICR spectra were fit to the data allowing for the determination of the cyclotron frequency. A sample of a $^{80}\text{Zr}^{16}\text{O}^+$ TOF-ICR spectrum and its theoretical line shape is shown in Fig. 1a.

Before and after each measurement of the ion of interest, measurements of a reference ion were performed to calibrate the magnetic field. The reference ions ($^{41}\text{K}^+$, $^{85,87}\text{Rb}^+$) were provided by an offline ion source. The masses of the ions of interest were obtained from the ratio (R) between cyclotron frequencies of the reference ion

($\nu_{c,\text{ref}}$) and the ion of interest:

$$R = \frac{\nu_{c,\text{ref}}}{\nu_c} = \frac{m_{\text{ion}}/q_{\text{ion}}}{(m_{\text{ref}} - q_{\text{ref}} \cdot m_e)/q_{\text{ref}}}, \quad (1)$$

where q_{ion} is the charge state of the ion of interest, and m_e is the mass of the electron, while m_{ref} and q_{ref} are the atomic mass and charge state of the reference species. The atomic mass m of the Zr isotope of interest is calculated from the mass of the measured ion, accounting for removed electrons and molecular counterparts, where applicable. The results of the measurements are displayed in Table I and compared to the Atomic Mass Evaluation of 2020 (AME20)²³. Further details on the measurement, calibration, and uncertainty determination procedures are given in Methods.

Our mass measurement results are in good agreement with the mass values recommended by AME20²³, and provide an improvement of one order of magnitude or more to the precision of the $^{80,81,83}\text{Zr}$ masses. The AME20 values for $^{81-83}\text{Zr}$ are derived mainly from previous high precision mass measurements. Penning trap mass measurements of $^{82,83}\text{Zr}$ form the basis of the AME20 mass values for these isotopes^{25,26}, while a recent storage ring measurement²⁷ dominates the AME20 mass of ^{81}Zr . Our measurement of ^{82}Zr has the largest discrepancy from AME20 with a value 1.5σ lower. The mass of ^{80}Zr listed in AME20 is an extrapolated value calculated from neighbouring known nuclei using smooth trends of the mass surface. It is worth noting that two previous mass measurements of ^{80}Zr have not been included in the AME. A measurement with only a single

Table I. **Results from our mass measurements.** The mass excesses are relative to the atomic mass of the isotopes of interest. The average frequency ratio (\bar{R}) between the ion of interest (Ion) and the reference ion (Ion Ref.) is presented. The results are also compared to the mass excesses recommended by the AME20²³. All mass excesses are in keV/ c^2 . 1 σ uncertainties are shown in parenthesis.

Isotope	Ion	Ion Ref.	\bar{R}	Mass Excess	AME20 ²³	Difference
⁸⁰ Zr	⁸⁰ Zr ¹⁶ O ⁺	⁸⁵ Rb ⁺	1.129 829 01 (99)	-55 128 (80)	-55 517 (1 500) ^a	389 (1 500)
⁸¹ Zr	⁸¹ Zr ²⁺	⁴¹ K ⁺	0.987 971 08 (13)	-57 556 (10)	-57 524 (92)	-32 (93)
⁸² Zr	⁸² Zr ¹⁶ O ⁺	⁸⁷ Rb ⁺	1.126 770 338 (31)	-63 618.6 (2.5)	-63 614.1 (1.6)	-4.5 (3.0)
⁸³ Zr	⁸³ Zr ²⁺	⁴¹ K ⁺	1.012 274 829 7 (85)	-65 916.33 (65)	-65 911.7 (6.4)	-4.7 (6.5)

^a Experimental result based on one ⁸⁰Zr event²⁴, not included in the AME20.

event²⁴ yielded a mass uncertainty of 1.5 MeV/ c^2 . The second measurement²⁸, albeit significantly more precise, has not been included in the AME because other isotopes measured in the same experiment were in disagreement with more recent high-precision results.

The Anomalous Mass of ⁸⁰Zr

Our mass measurement of ⁸⁰Zr reveals that this nucleus is significantly more bound than expected from systematic trends. Indeed, high-quality extrapolations of the mass surface towards ⁸⁰Zr have been produced by the AME collaboration and others; this has been especially motivated by the astrophysical significance of this nucleus for X-ray bursts²⁹. Our mass value is 370 keV/ c^2 more bound than the extrapolated value from AME20²³, and 950 keV/ c^2 more bound than the Lanzhou extrapolated value²⁷.

To study the impact of our new masses we employed various binding-energy differences described in Methods. Along the $N = Z$ line, nuclei are known to be exceptionally well bound as neutrons and protons occupy the same shell model orbitals. Therefore, a useful indicator is the double mass difference δV_{pn} ^{30,31} defined in Methods.

In Figure 2a and 2b, we show δV_{pn} for the $N = Z + 2$ and $N = Z$ sequences, respectively. For nuclei away from $N = Z$, the overall behaviour of δV_{pn} is well described by the macroscopic mass formula^{31,32} (MMF): $\delta V_{pn} \approx 2(a_{\text{sym}} + a_{\text{ssym}}A^{-1/3})/A$, where a_{sym} and a_{ssym} are, respectively, symmetry and surface-symmetry energy coefficients. In the MMF plotted in Figure 2a, we employed $a_{\text{sym}} = 35$ MeV and $a_{\text{ssym}} = -59$ MeV, which were determined through a fit to the data neglecting the outliers at $A = 58, 82, 102$. Along the $N = Z$ sequence, δV_{pn} is strongly impacted by the Wigner energy¹³, whose behaviour is more convoluted. Moreover, mass data beyond $N = Z$ are scarce in the investigated region. Consequently, if some masses required for the δV_{pn} determination were not experimentally available, we used the recommended values from AME20²³ instead.

Although δV_{pn} is expected to vary smoothly overall, fluctuations around the average trend carry important structural information^{30,31,33}. Binding-energy outliers, especially those found in magic nuclei along the $N = Z$ line, result in δV_{pn} deviations for both $N = Z$ and $N = Z + 2$ sequences. Considering the $N = Z + 2$ results

with our new masses, the value of δV_{pn} for ⁸²Zr (which is reliant on the mass of ⁸⁰Zr) is a clear outlier, being 185 keV lower than the MMF trend. This anomaly is similar to those found in ⁵⁸Ni and ¹⁰²Sn, associated with the increased binding energies of the doubly-magic self-conjugate nuclei ⁵⁶Ni and ¹⁰⁰Sn. The increased binding energy of ⁸⁰Zr also impacts the $N = Z$ trends resulting in increasing values of δV_{pn} for Zr and Mo.

Analogous outliers can also be found inspecting other mass filters at ⁸⁰Zr, such as the 2-proton shell gap δ_{2p} , commonly employed in tests of shell closures^{34,35}. See Methods Figure 1 for additional discussion.

The results shown in Figure 2 provide compelling empirical evidence for the existence of a deformed shell closure in ⁸⁰Zr. One needs to bear in mind, however, that ⁸⁰Zr is a self-conjugate system and some additional contribution to its binding energy comes from the Wigner energy. Usually, the Wigner term in even-even nuclei is parametrized as $E_W = a_W|N - Z|/A$. As discussed in Ref.¹³ and Methods, the Wigner-energy coefficient $W(A) = a_W/A$ can be empirically extracted from the values of δV_{pn} . Our data, shown in Figure 3, indicates that the value of $W(A)$ at ⁸⁰Zr and ⁵⁶Ni is locally enhanced, contrary to the gradually decreasing trend for heavier $N = Z$ nuclei that is well captured by the value of $a_W = 47$ MeV obtained in Ref.¹³. A note of caution is in order: some contribution to the local increase of the empirical value of W in ⁸⁰Zr and ⁵⁶Ni can be attributed to the enhanced binding due to their shell structure. The strength of the enhancement can be evaluated through another mass filter.

Experimental masses offer a way to assess the size of the deformed $N = 40$ single particle gap. This can be done by employing the filter $\Delta e(N = 2n)$ ³⁶, which provides an estimate of the single-particle energy gap $e_{n+1} - e_n$ at the Fermi level. Figure 4 shows Δe for the Zr isotopic chain (cf. Ref.³⁷ for the applications of Δe to the K and Ca chains). Some masses of proton-rich Zr isotopes needed to determine Δe are not known experimentally; those have been taken from mass relations of mirror nuclei by Zong et al.³⁸. It is seen that Δe reaches a maximum for ⁹⁰Zr at the spherical magic number $N = 50$ and a local maximum for ⁸⁰Zr at the deformed magic number $N = 40$. Since the latter value can be affected by the Wigner energy, we removed the

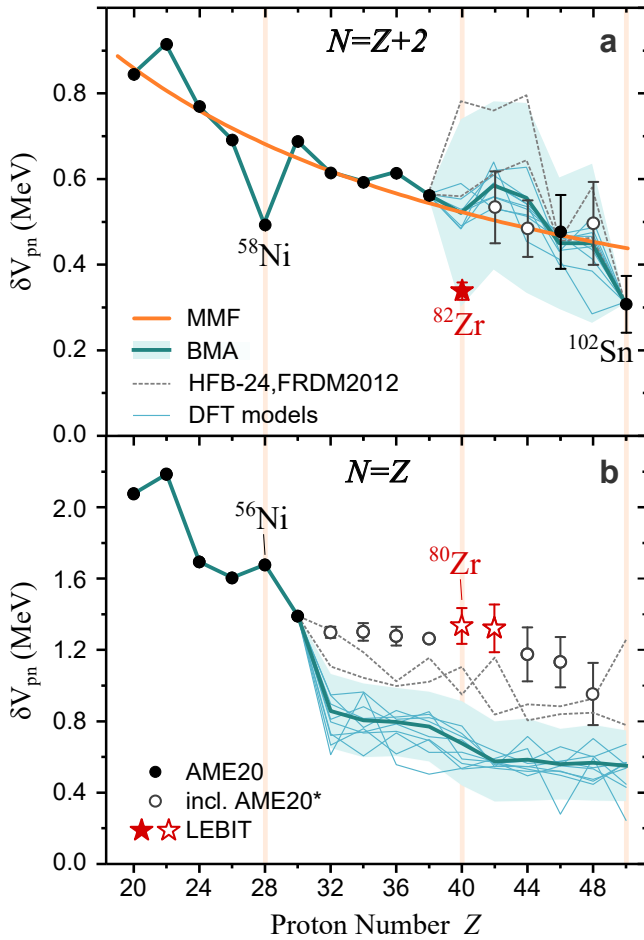


Figure 2. **Comparison of experimental results with theoretical predictions.** The effect of the anomalous mass of ^{80}Zr on the mass indicator δV_{pn} : a significant decrease from the baseline in the $N = Z + 2$ sequence (a), and a corresponding rise in the $N = Z$ sequence (b), which mirrors the behaviour of other doubly-magic nuclei (e.g. ^{56}Ni and ^{100}Sn). Black circles represent mass data from the AME20²³. Red stars include data from this work. Open symbols include mass extrapolations (AME20*) from AME20²³. The MMF prediction is marked by an orange line in (a). The thick teal line is the BMA result based on several nuclear models (thin solid lines: DFT models; thin dashed lines: HFB-24 and FRDM2012 models that include the Wigner-energy correction), and the light teal band represents the uncertainty of the BMA approach. See Methods for details on the BMA.

binding-energy contribution from E_W by applying two models: $E_W(1)$ ³⁹ and $E_W(2)$ ¹³. The resulting correction to Δe practically affects the $N = 40$ value only. As discussed in Methods, the expression $E_W(1)$ is well localized at $N = Z$ and reduces Δe by about 300 keV. The expression $E_W(2)$ decreases linearly with the neutron excess and the corresponding reduction of Δe is about 1.1 MeV. Even in this case, the energy gap at $N = 40$ is a factor of 2-3 larger than Δe for $42 \leq N \leq 48$. While the size of this gap is reduced as compared to the spherical $N = 50$ gap, it is characteristic of a deformed shell closure. The

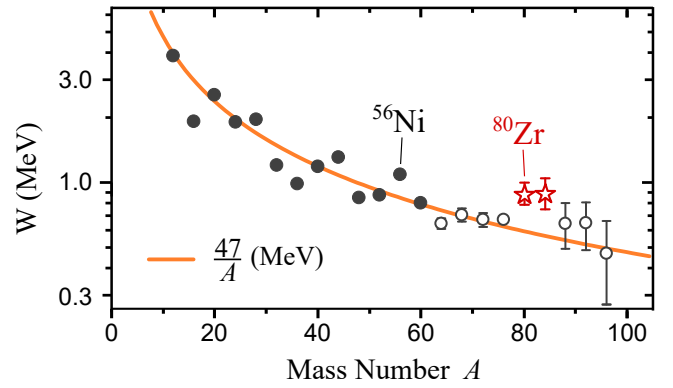


Figure 3. **Wigner energy.** The Wigner-energy coefficient $W(A)$ extracted from δV_{pn} values according to Ref.¹³. Black circles represent the mass data from the AME20²³. Red stars include data from this work. Open symbols (AME20*) include mass extrapolations. The average trend of Ref.¹³ is shown by a thick line.

strong shell effect comes from the self-conjugate nature of ^{80}Zr as the deformed proton and neutron shell effects reinforce one another.

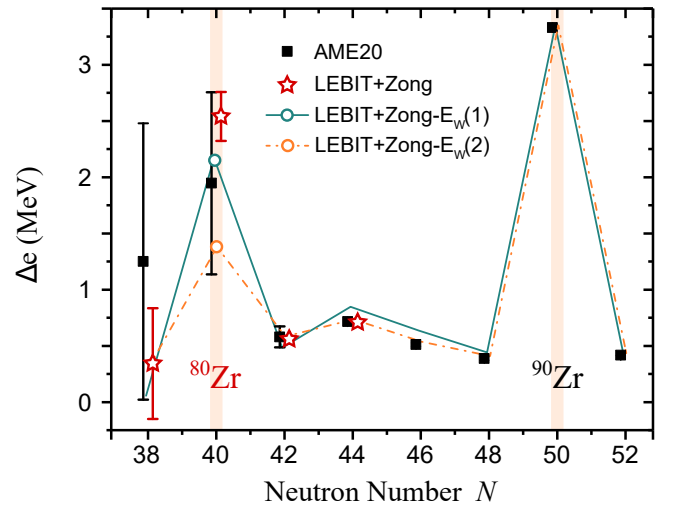


Figure 4. **Single-particle energy splitting.** The empirical single-particle energy gap $\Delta e(N)$ at the Fermi level for the chain of even-even Zr isotopes extracted from nuclear binding energies according to Ref.³⁶. Black squares represent the mass data from the AME20²³. Open stars represent the data from this work augmented by mass extrapolations from Ref.³⁸. These values of Δe were further corrected by removing contributions from the Wigner energy term $E_W(1)$ (solid line; Ref.³⁹) or $E_W(2)$ (dash-dotted line; Ref.¹³), cf. Methods for definition of E_W . Magic shell closures are seen at $N = 40$ and $N = 50$.

Bayesian Analysis of Mass Models

To obtain improved theoretical mass predictions in the ^{80}Zr region, we conducted a Bayesian statistical analysis combining Gaussian process extrapolation and Bayesian

Model Averaging (BMA)⁴⁰ of eleven theoretical global mass models following the same procedure as in Ref.¹⁵. The BMA framework uses the collective wisdom of the models, constrained by data, to make predictions and quantify uncertainties. Details on the individual models and the BMA methodology can be found in Methods.

The BMA predictions for δV_{pn} are shown in Figure 2a,b. The predictions for $N = Z + 2$ are well constrained outside the region $38 < Z < 50$ due to the wealth of experimental mass data. In the region $38 \leq Z \leq 50$, the BMA results are consistent with the AME20 data and the MMF trend. At $Z = 40$, the experimental δV_{pn} value, which includes our new $^{80,82}\text{Zr}$ mass results, falls just within the error band. The BMA result for δV_{pn} along $N = Z$ line in the region $Z > 30$ does not agree with either the AME20 extrapolations or the new experimental value at $Z = 40$. Two of the models, FRDM2012⁴¹ and HFB-24³⁹, that include the phenomenological Wigner term perform slightly better than the DFT models. However, they still fall short of the experimental trends, most likely due to underestimated Wigner energy. Indeed, the value of a_W in FRDM2012⁴¹ is 30 MeV, which is significantly less than $a_W = 47$ MeV representing the average trend seen in Figure 3. The Wigner energy $E_W(1)$ of HFB-24 is even smaller.

Conclusions

The high precision mass measurements of $^{80-83}\text{Zr}$ performed at the LEBIT facility allow a more detailed investigation of the mass surface in the region of strongly deformed nuclei with $N \approx Z \approx 40$. Our measurement reveals a significant enhancement in the binding energy of ^{80}Zr . By considering binding-energy indicators, we attribute this enhancement to a deformed double shell closure and an increase in the Wigner energy of this exotic self-conjugate system. A Bayesian average based on eleven global mass models was unable to account for the new mass value of ^{80}Zr as the Wigner-energy enhancement has not been taken into account microscopically. The comparisons to theory demonstrate the importance of accounting for the competition between deformation effects, isospin breaking effects, and proton-neutron pairing.

The interplay between theory and experiment was crucial in understanding this region of the nuclear chart. While the deformed shell gap at $N = Z = 40$ was predicted over 30 years ago^{4,5}, a lack of precise experimental data prevented a quantitative assessment of the gap's size until now. To further refine the deformed shell closure, high precision mass measurements in this region are needed, which will be made possible with next-generation radioactive ion beam facilities and mass measurement techniques.

Exploring the Heart of Matter (The National Academies Press, Washington, DC, 2013). URL <https://www.nap.edu/catalog/13438/nuclear-physics-exploring-the-heart-of-matter>.

- [2] Otsuka, T., Gade, A., Sorlin, O., Suzuki, T. & Utsuno, Y. Evolution of shell structure in exotic nuclei. *Rev. Mod. Phys.* **92**, 015002 (2020). URL <https://link.aps.org/doi/10.1103/RevModPhys.92.015002>.
- [3] Eberth, J., Meyer, R. A. & Sistemich, K. (eds.). *Nuclear Structure of the Zirconium Region* (Springer Berlin Heidelberg, Berlin, Heidelberg, 1988). URL <https://link.springer.com/book/10.1007/978-3-642-73958-3>.
- [4] Hamilton, J. H. *et al.* Effects of reinforcing shell gaps in the competition between spherical and highly deformed shapes. *J. Phys. G* **10**, L87–L91 (1984). URL <https://doi.org/10.1088/0305-4616/10/5/001>.
- [5] Nazarewicz, W., Dudek, J., Bengtsson, R., & Ragnarsson, I. Microscopic study of the high-spin behaviour in selected $A \simeq 80$ nuclei. *Nucl. Phys. A* **435**, 397 – 447 (1985). URL <http://www.sciencedirect.com/science/article/pii/0375947485904713>.
- [6] Petrovici, A., Schmid, K. & Faessler, A. Shape coexistence and shape transition in $N \approx Z$ nuclei from krypton to molybdenum. *Nucl. Phys. A* **605**, 290–300 (1996). URL <https://www.sciencedirect.com/science/article/pii/0375947496002242>.
- [7] Gaudefroy, L. *et al.* Collective structure of the $N = 40$ isotones. *Phys. Rev. C* **80**, 064313 (2009). URL <https://link.aps.org/doi/10.1103/PhysRevC.80.064313>.
- [8] Rodríguez, T. R. & Egido, J. L. Multiple shape coexistence in the nucleus ^{80}Zr . *Phys. Lett. B* **705**, 255 – 259 (2011). URL <http://www.sciencedirect.com/science/article/pii/S0370269311012354>.
- [9] Kaneko, K., Shimizu, N., Mizusaki, T. & Sun, Y. Triple enhancement of quasi-SU(3) quadrupole collectivity in Strontium-Zirconium $N \approx Z$ isotopes. *Phys. Lett. B* **817**, 136286 (2021). URL <https://www.sciencedirect.com/science/article/pii/S0370269321002264>.
- [10] Reinhard, P.-G. *et al.* Shape coexistence and the effective nucleon-nucleon interaction. *Phys. Rev. C* **60**, 014316 (1999). URL <https://link.aps.org/doi/10.1103/PhysRevC.60.014316>.
- [11] Lister, C. J. *et al.* Gamma radiation from the $N = Z$ nucleus $^{80}_{40}\text{Zr}_{40}$. *Phys. Rev. Lett.* **59**, 1270–1273 (1987). URL <https://link.aps.org/doi/10.1103/PhysRevLett.59.1270>.
- [12] Llewellyn, R. D. O. *et al.* Establishing the Maximum Collectivity in Highly Deformed $N = Z$ Nuclei. *Phys. Rev. Lett.* **124**, 152501 (2020). URL <https://link.aps.org/doi/10.1103/PhysRevLett.124.152501>.
- [13] Satula, W., Dean, D., Gary, J., Mizutori, S. & Nazarewicz, W. On the origin of the Wigner energy. *Phys. Lett. B* **407**, 103–109 (1997). URL <https://www.sciencedirect.com/science/article/pii/S0370269397007119>.
- [14] Bentley, I. & Frauendorf, S. Relation between Wigner energy and proton-neutron pairing. *Phys. Rev. C* **88**, 014322 (2013). URL <https://link.aps.org/doi/10.1103/PhysRevC.88.014322>.
- [15] Neufcourt, L. *et al.* Quantified limits of the nuclear landscape. *Phys. Rev. C* **101**, 044307 (2020). URL <https://link.aps.org/doi/10.1103/PhysRevC.101.044307>.
- [16] König, M., Bollen, G., Kluge, H.-J., Otto, T. & Szerypo, J. Quadrupole excitation of stored ion motion at the true cyclotron frequency. *Int. J. Mass Spectrom. Ion Process.*

[1] National Research Council. *Nuclear Physics:*

- 142, 95–116 (1995). URL <https://www.sciencedirect.com/science/article/pii/016811769504146C>.
- [17] ENSDF. Evaluated Nuclear Structure Data File (2021). URL <https://www.nndc.bnl.gov/ensarchivals>. Data extracted using the National Nuclear Data Center On-Line Data Service from the ENSDF database, file revised as of 04 Jan 2021.
- [18] Morrissey, D., Sherrill, B., Steiner, M., Stolz, A. & Wiedenhoever, I. Commissioning the A1900 projectile fragment separator. *Nucl. Instrum. Methods Phys. Res. B* **204**, 90 – 96 (2003). URL <http://www.sciencedirect.com/science/article/pii/S0168583X02018955>. 14th International Conference on Electromagnetic Isotope Separators and Techniques Related to their Applications.
- [19] Lund, K. *et al.* Online tests of the Advanced Cryogenic Gas Stopper at NSCL. *Nucl. Instrum. Methods Phys. Res. B* **463**, 378 – 381 (2020). URL <http://www.sciencedirect.com/science/article/pii/S0168583X1930237X>.
- [20] Ringle, R., Schwarz, S. & Bollen, G. Penning trap mass spectrometry of rare isotopes produced via projectile fragmentation at the LEBIT facility. *Int. J. Mass Spectrom.* **349-350**, 87 – 93 (2013). URL <http://www.sciencedirect.com/science/article/pii/S1387380613001279>. 100 years of Mass Spectrometry.
- [21] Schwarz, S., Bollen, G., Ringle, R., Savory, J. & Schury, P. The LEBIT ion cooler and buncher. *Nucl. Instrum. Methods Phys. Res. A* **816**, 131 – 141 (2016). URL <http://www.sciencedirect.com/science/article/pii/S0168900216001194>.
- [22] Ringle, R. *et al.* The LEBIT 9.4T Penning trap mass spectrometer. *Nucl. Instrum. Methods Phys. Res. A* **604**, 536 – 547 (2009). URL <http://www.sciencedirect.com/science/article/pii/S0168900209006901>.
- [23] Huang, W., Wang, M., Kondev, F., Audi, G. & Naimi, S. The AME 2020 atomic mass evaluation (I). Evaluation of input data, and adjustment procedures*. *Chin. Phys. C* **45**, 030002 (2021). URL <https://doi.org/10.1088/1674-1137/abddb0>.
- [24] Issmer, S. *et al.* Direct mass measurements of A=80 isobars. *Eur. Phys. J. A* **2**, 173 – 177 (1998). URL <https://doi.org/10.1007/s100500050106>.
- [25] Kankainen, A. *et al.* Mass measurements of neutron-deficient nuclides close to A = 80 with a Penning trap. *Eur. Phys. J. A* **29**, 271 – 280 (2006). URL <https://doi.org/10.1140/epja/i2006-10088-6>.
- [26] Vilén, M. *et al.* High-precision mass measurements and production of neutron-deficient isotopes using heavy-ion beams at IGISOL. *Phys. Rev. C* **100**, 054333 (2019). URL <https://link.aps.org/doi/10.1103/PhysRevC.100.054333>.
- [27] King, Y. *et al.* Mass measurements of neutron-deficient Y, Zr, and Nb isotopes and their impact on rp and ν p nucleosynthesis processes. *Phys. Lett. B* **781**, 358–363 (2018). URL <https://www.sciencedirect.com/science/article/pii/S0370269318302934>.
- [28] Lalleman, A. S. *et al.* Mass Measurements of Exotic Nuclei around $N = Z = 40$ with CSS2. *Hyp. Interac.* **132**, 313 – 320 (2001). URL <https://doi.org/10.1023/A:1011928521373>.
- [29] Schatz, H. & Ong, W.-J. Dependence of X-Ray Burst Models on Nuclear Masses. *Astrophys. J.* **844**, 139 (2017). URL <https://doi.org/10.3847/2F1538-4357/2Faa7de9>.
- [30] Zhang, J.-Y., Casten, R. & Brenner, D. Empirical proton-neutron interaction energies. Linearity and saturation phenomena. *Phys. Lett. B* **227**, 1–5 (1989). URL <https://www.sciencedirect.com/science/article/pii/0370269389912732>.
- [31] Stoitsov, M., Cakirli, R. B., Casten, R. F., Nazarewicz, W. & Satulá, W. Empirical Proton-Neutron Interactions and Nuclear Density Functional Theory: Global, Regional, and Local Comparisons. *Phys. Rev. Lett.* **98**, 132502 (2007). URL <https://link.aps.org/doi/10.1103/PhysRevLett.98.132502>.
- [32] Reinhard, P.-G., Bender, M., Nazarewicz, W. & Vertse, T. From finite nuclei to the nuclear liquid drop: Leptodermous expansion based on self-consistent mean-field theory. *Phys. Rev. C* **73**, 014309 (2006). URL <https://link.aps.org/doi/10.1103/PhysRevC.73.014309>.
- [33] Bender, M. & Heenen, P.-H. What can be learned from binding energy differences about nuclear structure: The example of δV_{pn} . *Phys. Rev. C* **83**, 064319 (2011). URL <https://link.aps.org/doi/10.1103/PhysRevC.83.064319>.
- [34] Bender, M. *et al.* The $Z = 82$ shell closure in neutron-deficient Pb isotopes. *Eur. Phys. J. A* **14**, 23–28 (2002). URL <https://doi.org/10.1140/epja/iepja1320>.
- [35] Lunney, D., Pearson, J. M. & Thibault, C. Recent trends in the determination of nuclear masses. *Rev. Mod. Phys.* **75**, 1021–1082 (2003). URL <https://link.aps.org/doi/10.1103/RevModPhys.75.1021>.
- [36] Satulá, W., Dobaczewski, J. & Nazarewicz, W. Odd-Even Staggering of Nuclear Masses: Pairing or Shape Effect? *Phys. Rev. Lett.* **81**, 3599–3602 (1998). URL <https://link.aps.org/doi/10.1103/PhysRevLett.81.3599>.
- [37] Koszorús, Á. *et al.* Charge radii of exotic potassium isotopes challenge nuclear theory and the magic character of $N = 32$. *Nat. Phys.* **17**, 439–443 (2021). URL <https://doi.org/10.1038/s41567-020-01136-5>.
- [38] Zong, Y. Y., Ma, C., Zhao, Y. M. & Arima, A. Mass relations of mirror nuclei. *Phys. Rev. C* **102**, 024302 (2020). URL <https://link.aps.org/doi/10.1103/PhysRevC.102.024302>.
- [39] Gorieli, S., Chamel, N. & Pearson, J. M. Further explorations of Skyrme-Hartree-Fock-Bogoliubov mass formulas. XIII. The 2012 atomic mass evaluation and the symmetry coefficient. *Phys. Rev. C* **88**, 024308 (2013). URL <https://link.aps.org/doi/10.1103/PhysRevC.88.024308>.
- [40] Phillips, D. R. *et al.* Get on the BAND wagon: A Bayesian framework for quantifying model uncertainties in nuclear dynamics. *J. Phys. G* (2021). URL <http://iopscience.iop.org/article/10.1088/1361-6471/abf1df>.
- [41] Möller, P., Sierk, A., Ichikawa, T. & Sagawa, H. Nuclear ground-state masses and deformations: FRDM(2012). *Atom. Data Nucl. Data Tables* **109-110**, 1 – 204 (2016). URL <http://www.sciencedirect.com/science/article/pii/S0092640X1600005X>.

METHODS

The TOF-ICR technique for cyclotron frequency determination

In a Penning trap, an ion is confined in space by the superposition of a weak axially-harmonic electric potential and a strong homogeneous magnetic field, oriented in the axial direction. In the absence of the electric field, the ion performs a circular motion about the axis of the magnetic field at the cyclotron frequency ν_c , whose measurement allows for the determination of the mass of the particle. The introduction of the electric field disturbs the cyclotron motion, which is split into two independent radial components: the reduced cyclotron and the much slower magnetron precession (with frequencies ν_+ and ν_- , respectively). The “free” cyclotron frequency is determined by the measurement of the $\nu_c = \nu_+ + \nu_-$ sideband. This quantity is nearly invariant with respect to fluctuations in the trapping electric field, which grants Penning trap mass spectrometry great accuracy⁴².

In the TOF-ICR technique, the sideband is determined by applying an external quadrupole radiofrequency field (with frequency ν_{RF}) to the ion that converts one eigenmotion into the other. The ion is initially prepared in a pure magnetron motion, which, at LEBIT, is done through the Lorentz steering technique⁴³. Upon the application of the external field, if the resonant condition $\nu_{RF} = \nu_+ + \nu_-$ is met, the conversion from pure magnetron motion to pure reduced cyclotron motion occurs. The conversion is probed by measuring the ion’s time of flight from the trap to a microchannel plate detector outside of the magnetic field. If the ion in the trap is in a pure reduced cyclotron motion, which holds greater kinetic energy, the time of flight is significantly shorter. The LEBIT Facility section of Figure 1 provides a schematic of the TOF-ICR setup.

In a typical TOF-ICR procedure, ν_{RF} is scanned to characterize the resonant reduction of the time of flight, generating spectra such as the one shown in Figure 1a. The width of the resonance, which determines the precision of the ν_c measurement, is inversely proportional to the time which the external excitation field is applied. In the measurements described herein, both continuous¹⁶ and Ramsey⁴⁴ radiofrequency quadrupolar excitation schemes were used with excitation times ranging from 50 ms to 1 s. The cyclotron frequency is determined through an analytical fit to the time of flight spectrum, whose line shapes are described in the literature for both excitation schemes employed^{16,44}.

Mass determination from cyclotron frequencies

Here we describe in greater detail the procedure employed to extract atomic mass values for the isotopes of interest from the measured cyclotron frequencies. As explained in the main text, each measurement of the ion of interest’s cyclotron frequency ν_c was interleaved by measurements of the cyclotron frequency of the reference ion, $\nu_{c,\text{ref}}$. Reference ions were chosen as singly ionized species of widely available stable alkali atoms whose

masses (m_{ref}) are well known in the literature²³, as well as whose A/Q was close to the ion of interest to avoid large mass-dependent systematic shifts in the calibration procedure. The frequency ratio (1) for each measurement of ν_c was calculated using the time-interpolated cyclotron frequency from the reference measurements to the time of the measurement of the ion of interest. In total, 3 measurements of R were performed of the $^{83}\text{Zr}^{2+}-^{41}\text{K}^+$ pair, 6 of the $^{82}\text{ZrO}^+-^{87}\text{Rb}^+$ pair, 5 of the $^{81}\text{Zr}^{2+}-^{41}\text{K}^+$ pair, and 4 of the $^{80}\text{ZrO}^+-^{85}\text{Rb}^+$ pair. The masses of each ion of interest (m_{ion}) were calculated through Eq.(1) using the average of multiple frequency ratios (\bar{R}), presented in Table I.

The atomic masses (m) of the Zr isotopes of interest were calculated using $m = m_{\text{ion}} + q \cdot m_e - m_{\text{mol}}$, where m_{mol} is the atomic mass of the molecular counterpart (^{16}O in the case of $^{80,82}\text{Zr}$ only). The electron binding energies and molecular binding energies of $^{80,82}\text{ZrO}^+$ were disregarded as they are on the order of eV, which is several orders of magnitude lower than the statistical uncertainty of the measurement. Mass excesses, defined as the difference between the atomic mass and the isotope’s mass number, are reported in Table I for the measured Zr isotopes.

Evaluation of uncertainties

Uncertainties related to the extraction of cyclotron frequencies from the fits dominate the statistical error budget. Most systematic uncertainties in the measured frequency ratio scale linearly with the mass difference between the ion of interest and the reference ion. These systematic effects include magnetic field inhomogeneities, trap misalignment with the magnetic field, and anharmonic imperfections in the trapping potential⁴⁵. The mass-dependent shifts in \bar{R} have been measured at the LEBIT facility and found to be $\Delta\bar{R} = 2 \times 10^{-10}/u$ ⁴⁶. This shift has been folded into the ratios and uncertainties reported in Table I.

Remaining systematic effects include nonlinear time-dependent changes in the magnetic field, relativistic effects on the cyclotron frequency, and ion-ion interactions in the trap. Previous work has shown that the effect of nonlinear magnetic field fluctuations on the individual ratios R are less than 1×10^{-9} over an hour⁴⁷. Measurement times ranged from three hours for ^{80}Zr to fifteen minutes for ^{83}Zr . This uncertainty was also folded into the ratio uncertainties though it had a negligible effect on the final error estimate. The relativistic effects on the cyclotron frequency ratio⁴⁸ were negligible compared to the statistical uncertainty. Ion-ion interactions were minimized using several methods. Before entering the trap, the ion bunches from the cooler and buncher were purified using a time-of-flight filter to only allow ions with a specific mass-to-charge ratio to enter the trap. Once captured in the trap, ions were further purified against isobaric contamination using targeted dipole cleaning⁴⁹ and the stored waveform inverse Fourier Transform (SWIFT) technique⁵⁰. Additional ion-ion interactions were taken

into account by performing a count-rate class analysis on each data set whenever possible⁵¹. The count-rate class analysis only led to a shift in the ^{83}Zr ratio ($\Delta R = 9.8(7) \times 10^{-9}$). This shift has been included in the value reported in Table I. Finally, Birge ratios were calculated to determine whether inner or outer uncertainties were reported for the final mass uncertainties⁵².

Binding-energy indicators

To extract quantities of interest for the experimental mass surface, we employ various binding-energy differences (mass filters)^{53,54}. Those include:

The double mass difference δV_{pn} ^{30,31,33}:

$$\delta V_{pn}(N, Z) = \frac{1}{4}[B(N, Z) - B(N-2, Z) - B(N, Z-2) + B(N-2, Z-2)]; \quad (1)$$

The Wigner energy coefficient in an even-even nucleus with $N = Z = A/2$ ¹³:

$$W(A) = \delta V_{pn}(A/2, A/2) - \frac{1}{2}[\delta V_{pn}(A/2, A/2-2) + \delta V_{pn}(A/2+2, A/2)]; \quad (2)$$

The two-proton shell gap δ_{2p} ^{34,35}:

$$\delta_{2p}(N, Z) = 2B(N, Z) - B(N, Z+2) - B(N, Z-2); \quad (3)$$

The three-point mass difference $\Delta_n^{(3)}$ ³⁶:

$$\Delta_n^{(3)}(N, Z) = \frac{(-1)^N}{2}[2B(N, Z) - B(N-1, Z) - B(N+1, Z)]; \quad (4)$$

The single-particle energy splitting Δe ³⁶:

$$\Delta e(N, Z) = e_{n+1} - e_n = 2[\Delta_n^{(3)}(N = 2n, Z) - \Delta_n^{(3)}(N = 2n+1, Z)]. \quad (5)$$

In the above equations, B is the (positive) nuclear binding energy, obtained from the atomic mass of the nucleus.

Wigner-energy parametrizations

The Wigner energy contribution to the total binding energy produces an additional binding for nuclei close to $N = Z$. In the HFB-24 mass model³⁹, the Wigner term has been parametrized as:

$$E_W(1) = V_W e^{-\lambda w \left(\frac{N-Z}{A}\right)^2} + V'_W |N - Z| e^{-\left(\frac{A}{A_0}\right)^2}, \quad (6)$$

where $V_W = 1.8$ MeV, $\lambda w = 380$, $V'_W = -0.84$ MeV, and $A_0 = 26$. In this model, E_W rapidly decreases with $|N - Z|$ when moving away from the $N = Z$ line. In the traditional parametrization of E_W ,

$$E_W(2) = -a_W \frac{|N - Z|}{A}, \quad (7)$$

one assumes that $E_W = 0$ at $N = Z$ and linearly decreases with the neutron excess. In this work, we adopt the value of $a_W = 47$ MeV from Ref.¹³.

Nuclear models

In this study we considered 9 models based on nuclear density functional theory (DFT): SkM^{*}⁵⁵, SkP⁵⁶, SLy4⁵⁷, SV-min⁵⁸, UNEDF0⁵⁹, UNEDF1⁶⁰, UNEDF2⁶¹, D1M⁶², and BCPM⁶³. Two additional mass models commonly used in nuclear astrophysics studies were also considered: FRDM2012⁴¹ and HFB-24³⁹.

Three of these models (SkM^{*}, UNEDF0 and FRDM2012) predict large prolate ground-state deformation for ^{80}Zr around $\beta_2 = 0.39$, in agreement with experiment. HFB-24 predicts an oblate deformed ground state while all the remaining models predict a spherical ground state. Such variations in the predicted ground-state deformation are manifestations of near-lying coexisting configurations with different shapes expected theoretically, as discussed in the main text. It is important to notice that while the relative position between the different minima strongly depends on the underlying interaction¹⁰ and beyond-DFT correlations⁸, the energy shifts between the deformed ground-state configuration and the spherical minimum is relatively small¹⁰. As a consequence, the absolute impact of shape coexistence in the predicted mass value is expected to be minor and can be absorbed by the statistical correction.

Bayesian Model Averaging

The binding energies $B(N, Z)$ predicted by nuclear mass models were used to compute the two-proton separation energies:

$$S_{2p}(N, Z) = B(N, Z) - B(N, Z-2), \quad (8)$$

which were then used to compute δV_{pn} mass differences.

For each model employed, we construct the statistical emulator $\delta_{S_{2p}}^{\text{em}}$ of separation energy residuals:

$$\delta_{S_{2p}}^{\text{em}}(N, Z) := S_{2p}^{\text{exp}}(N, Z) - S_{2p}^{\text{th}}(N, Z). \quad (9)$$

The predicted separation energies are then given by $S_{2p}^{\text{em}}(N, Z) = S_{2p}^{\text{th}}(N, Z) + \delta_{S_{2p}}^{\text{em}}$. The training datasets were built from experimental masses from AME20 for even-even nuclei with $20 \leq Z \leq 50$ and the theoretical mass tables. Seven nuclei (^{48}Ni , ^{54}Zn , ^{84}Zr , ^{86}Mo , ^{90}Ru , ^{92}Ru , and ^{94}Pd) placed at the dataset outer boundary were excluded from the training set and used as independent testing data to compute the BMA evidence weights. Our dataset consists therefore of 152 points (x_i, y_i) , where $x := (N_i, Z_i)$ and $y_i := \delta_{S_{2p}}^{\text{em}}(x_i)$.

Following the Bayesian methodology described in Ref.¹⁵, we constructed emulators for separation energy residuals $\delta^{GP}(N, Z)$ using Gaussian Processes (GP) $\delta^{GP}(x) \sim \mathcal{GP}(\mu, k_{\eta, \rho}(x, x'))$ over the bi-dimensional domain x . The GP is characterized by its mean function and covariance kernel, taken respectively as a constant μ and squared-exponential covariance kernel $k_{\eta, \rho}(x, x') :=$

$\eta^2 e^{-\frac{(Z-Z')^2}{\rho_Z} - \frac{(N-N')^2}{\rho_N}}$, where ρ_Z and ρ_N are the correlation ranges along the proton and neutron direction, respectively. We add to the model a term accounting for statistical uncertainties, assumed independent, identically distributed and scaled by a parameter σ . This yields

$$y_i = \delta^{GP}(x_i) + \sigma \epsilon_i. \quad (10)$$

Thus our GP model is parametrized by the 5-dimensional vector $\theta := (\mu, \eta, \rho_Z, \rho_N, \sigma)$.

Posterior distributions for the \mathcal{GP} parameters are obtained via Bayes' equation

$$p(y|\theta) := \frac{p(\theta|y)\pi(\theta)}{\int p(\theta|y)\pi(\theta)d\theta}, \quad (11)$$

where $p(\theta|y)$ is the statistical model (10)'s likelihood and $\pi(\theta)$ the prior on its parameters. Priors we taken weakly informative, as described in Ref.¹⁵. Samples from the posterior distributions of the \mathcal{GP} parameters were drawn from iterations of a Monte Carlo Markov Chain. These samples of the residuals' emulators were in turn used to produce samples of two-proton separation energies and mass filters, as well as derive statistical predictions: averages and corresponding correlated uncertainties along with full covariance matrices.

In a second stage of the analysis, we ensemble the emulators built from each individual nuclear model according to their BMA weights, namely the posterior probability for each model to be the hypothetical *true* model, *assuming it is one of them*, given priors on model weights and data. While the classical BMA literature⁶⁴ relies on the same data y as used for the individual model's training, for this step we prefer to use new "testing" data y^* (⁴⁸Ni, ⁵⁴Zn, ⁸⁴Zr, ⁸⁶Mo, ⁹⁰Ru, ⁹²Ru, and ⁹⁴Pd) located at the outer boundary of the training set and excluded from the GP training. This ensures that the weights reflect better the extrapolative power of the models, and reduces overfitting. Formally we can write¹⁵ these BMA weights as

$$w_k = p(\mathcal{M}_k|y^*) = \frac{p(y^*|\mathcal{M}_k)\pi(\mathcal{M}_k)}{\sum_{\ell=1}^{11} p(y|\mathcal{M}_\ell)\pi(\mathcal{M}_\ell)}, \quad (12)$$

where $\pi(\mathcal{M}_k)$ are prior model weights, and $p(y|\mathcal{M}_k)$ are the model evidences obtained by integrating the likelihood equation over the parameter space. For our GP emulators, this gives

$$p(y|\mathcal{M}_k) = \int p(y|\theta_k, \mathcal{M}_k)\pi(\theta_k, \mathcal{M}_k)d\theta_k. \quad (13)$$

We assume uniform prior weights, which are from a statistical standpoint the unique non-informative prior distribution in this setup. In order to speed up computations and increase stability⁶⁵, the evidence integrals are calculated using the Laplace approximation⁶⁴, where it is assumed that the posterior is Gaussian with the same

mean and standard deviation. The resulting model evidences are:

$$p(y|\mathcal{M}_k) \approx \exp \left[- \sum_i \frac{(y_i^{exp} - y^{(k)}(x_i))^2}{2\sigma_{y_k}(x_i)^2} \right], \quad (14)$$

where $y^{(k)}$ are the individual model emulators' predictions, $\sigma_{y_k}(x)$ the corresponding uncertainties, and i runs over the retained set of nuclei⁶⁵.

The model weights (rounded to two decimal digits) are: $w_k=0.01$ (SkM*), 0.04 (SkP), 0.12 (SLy4), 0.16 (SV-min), 0.07 (UNEDF0), 0.11 (UNEDF1), 0.20 (UNEDF2), 0.05 (BCPM), 0.21 (D1M), 0.00 (FRDM), and 0.00 (HFB-24). The final BMA predictions and uncertainties are calculated as

$$y(x) = \sum_k w_k y^{(k)}(x);$$

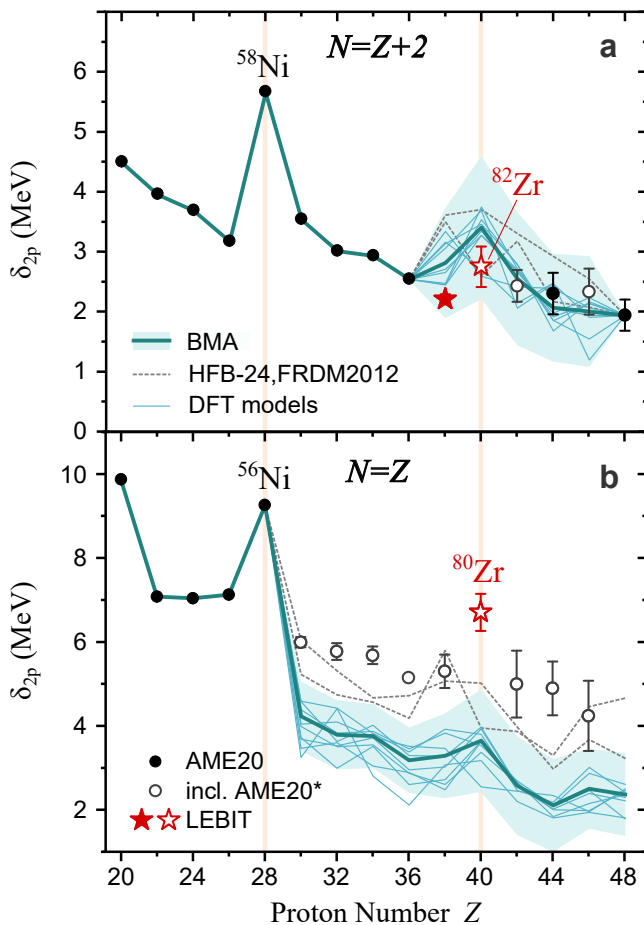
$$\sigma_y^2(x) = \sum_k w_k (y^{(k)}(x) - y(x))^2 + \sum_k w_k \sigma_{y_k}^2(x),$$

This last equation conveniently splits the uncertainties into the uncertainty on the model choice and the uncertainty on the individual models' parameters, and highlights what would be lost if a single model were used.

The two-proton shell gap

Figure 1 displays the two-proton shell gap δ_{2p} (3). For the $N = Z + 2$ sequence, the BMA prediction agrees with experiment within the estimated uncertainty. For $N = Z$, the anomalous mass of ⁸⁰Zr results in an increase of δ_{2p} above the baseline. Similar to what is seen in Figure 2b, the HFB-24 and FRDM2012 models that include the Wigner-energy correction lie slightly below the data points. As discussed earlier, this suggests that the Wigner energy term is underestimated by both models.

-
- [42] Gabrielse, G. Why Is Sideband Mass Spectrometry Possible with Ions in a Penning Trap? *Phys. Rev. Lett.* **102**, 172501 (2009). URL <https://link.aps.org/doi/10.1103/PhysRevLett.102.172501>.
- [43] Ringle, R. *et al.* A "Lorentz" steerer for ion injection into a Penning trap. *Int. J. Mass Spectrom.* **263**, 38–44 (2007). URL <https://www.sciencedirect.com/science/article/pii/S1387380606005781>.
- [44] George, S. *et al.* The Ramsey method in high-precision mass spectrometry with Penning traps: Experimental results. *Int. J. Mass Spectrom.* **264**, 110–121 (2007). URL <https://www.sciencedirect.com/science/article/pii/S1387380607001662>.
- [45] Bollen, G., Moore, R. B., Savard, G. & Stolzenberg, H. The accuracy of heavy-ion mass measurements using time of flight-ion cyclotron resonance in a Penning trap. *J. Appl. Phys.* **68**, 4355–4374 (1990). URL <https://doi.org/10.1063/1.346185>. <https://doi.org/10.1063/1.346185>.
- [46] Gulyuz, K. *et al.* Determination of the direct double- β -decay Q value of ⁹⁶Zr and atomic masses of



METHODS Figure 1. **Two-proton shell gap.** The effect of the anomalous mass of ^{80}Zr on the mass indicator δ_{2p} : a decrease from the baseline in the $N = Z + 2$ sequence (a), and a corresponding rise in the $N = Z$ sequence (b). Black circles represent mass data from the AME20²³. Red stars include data from this work. Open symbols include mass extrapolations from AME20²³. The thick teal line is the BMA result based on several nuclear models (thin solid lines: DFT models; thin dashed lines: HFB-24 and FRDM2012 models that include the Wigner-energy correction), and the light teal band represents the uncertainty of the BMA approach.

90–92,94,96Zr and 92,94–98,100Mo. *Phys. Rev. C* **91**, 055501 (2015). URL <https://link.aps.org/doi/10.1103/PhysRevC.91.055501>.

- [47] Ringle, R. *et al.* High-precision Penning trap mass measurements of $^{37,38}\text{Ca}$ and their contributions to conserved vector current and isobaric mass multiplet equation. *Phys. Rev. C* **75**, 055503 (2007). URL <https://link.aps.org/doi/10.1103/PhysRevC.75.055503>.
- [48] Brown, L. S. & Gabrielse, G. Geonium theory: Physics of a single electron or ion in a Penning trap. *Rev. Mod. Phys.* **58**, 233–311 (1986). URL <https://link.aps.org/doi/10.1103/RevModPhys.58.233>.
- [49] Blaum, K. *et al.* Population inversion of nuclear states by a Penning trap mass spectrometer. *Europhys. Lett.* **67**, 586–592 (2004). URL <https://doi.org/10.1209/epl/i2004-10089-5>.
- [50] Kwiatkowski, A. A., Bollen, G., Redshaw, M., Ringle,

R. & Schwarz, S. Isobaric beam purification for high precision Penning trap mass spectrometry of radioactive isotope beams with SWIFT. *Int. J. Mass Spectrom.* **379**, 9–15 (2015). URL <http://www.sciencedirect.com/science/article/pii/S1387380614004011>.

- [51] Bollen, G. *et al.* Resolution of nuclear ground and isomeric states by a Penning trap mass spectrometer. *Phys. Rev. C* **46**, R2140–R2143 (1992). URL <https://link.aps.org/doi/10.1103/PhysRevC.46.R2140>.
- [52] Birge, R. T. The Calculation of Errors by the Method of Least Squares. *Phys. Rev.* **40**, 207–227 (1932). URL <https://link.aps.org/doi/10.1103/PhysRev.40.207>.
- [53] Jänecke, J. & Comay, E. Properties of homogeneous and inhomogeneous mass relations. *Nucl. Phys. A* **436**, 108–124 (1985). URL <https://www.sciencedirect.com/science/article/pii/0375947485905445>.
- [54] Jensen, A., Hansen, P. & Jonson, B. New mass relations and two- and four-nucleon correlations. *Nucl. Phys. A* **431**, 393–418 (1984). URL <https://www.sciencedirect.com/science/article/pii/0375947484901167>.
- [55] Bartel, J., Quentin, P., Brack, M., Guet, C. & Håkansson, H.-B. Towards a better parametrisation of Skyrme-like effective forces: A critical study of the SkM force. *Nucl. Phys. A* **386**, 79–100 (1982). URL <https://www.sciencedirect.com/science/article/pii/0375947482904031>.
- [56] Dobaczewski, J., Flocard, H. & Treiner, J. Hartree-Fock-Bogolyubov description of nuclei near the neutron-drip line. *Nucl. Phys. A* **422**, 103–139 (1984). URL <https://www.sciencedirect.com/science/article/pii/0375947484904330>.
- [57] Chabanat, E., Bonche, P., Haensel, P., Meyer, J. & Schaeffer, R. New Skyrme effective forces for supernovae and neutron rich nuclei. *Phys. Scr.* **T56**, 231–233 (1995). URL <https://doi.org/10.1088/0031-8949/1995/t56/034>.
- [58] Klüpfel, P., Reinhard, P.-G., Bürvenich, T. J. & Maruhn, J. A. Variations on a theme by Skyrme: A systematic study of adjustments of model parameters. *Phys. Rev. C* **79**, 034310 (2009). URL <https://link.aps.org/doi/10.1103/PhysRevC.79.034310>.
- [59] Kortelainen, M. *et al.* Nuclear energy density optimization. *Phys. Rev. C* **82**, 024313 (2010). URL <https://link.aps.org/doi/10.1103/PhysRevC.82.024313>.
- [60] Kortelainen, M. *et al.* Nuclear energy density optimization: Large deformations. *Phys. Rev. C* **85**, 024304 (2012). URL <https://link.aps.org/doi/10.1103/PhysRevC.85.024304>.
- [61] Kortelainen, M. *et al.* Nuclear energy density optimization: Shell structure. *Phys. Rev. C* **89**, 054314 (2014). URL <https://link.aps.org/doi/10.1103/PhysRevC.89.054314>.
- [62] Goriely, S., Hilaire, S., Girod, M. & Péru, S. First Gogny-Hartree-Fock-Bogoliubov Nuclear Mass Model. *Phys. Rev. Lett.* **102**, 242501 (2009). URL <https://link.aps.org/doi/10.1103/PhysRevLett.102.242501>.
- [63] Baldo, M., Robledo, L. M., Schuck, P. & Viñas, X. New Kohn-Sham density functional based on microscopic nuclear and neutron matter equations of state. *Phys. Rev. C* **87**, 064305 (2013). URL <https://link.aps.org/doi/10.1103/PhysRevC.87.064305>.
- [64] Kass, R. E. & Raftery, A. E. Bayes Factors. *J. Am. Stat. Assoc.* **90**, 773–795 (1995). URL <https://www.tandfonline.com/doi/abs/10.1080/>

01621459.1995.10476572.

- [65] Kejzlar, V., Neufcourt, L., Maiti, T. & Viens, F. Bayesian averaging of computer models with domain discrepancies: a nuclear physics perspective (2019). URL <https://arxiv.org/abs/1904.04793>. 1904.04793.

Data availability

The data that support the plots within this paper and other findings of this study are available from the corresponding author upon reasonable request.

Code availability

Our unpublished computer codes used to generate results that are reported in the paper and central to its main claims will be made available upon request, to editors and reviewers.

Acknowledgements

The authors would like to thank the NSCL staff for their technical support as well as Richard F. Casten for useful discussions on interpreting the results of the experiment. This work was conducted with the support of Michigan State University, the U.S. National Science Foundation under Contract No. PHY-1565546, the U.S. Department of Energy, Office of Science, Office of Nuclear Physics under Award Nos. DE-SC0015927, DE-SC0013365, and DE-SC0018083 (NUCLEI SciDAC-4 collaboration), and by the National Science Foundation CSSI program under award number 2004601 (BAND collaboration).

Author contributions

A.H., E.L., G.B., K.L., C.N., D.P., R.R., C.S.S., and I.T.Y. performed the experiment. A.H., E.L., D.P., and I.T.Y. performed the data analysis. A.H., E.L., W.N., S.A.G., and L.N. prepared the manuscript. R.J., S.A.G., W.N., and L.N. performed the Bayesian analysis. All authors discussed the results and provided comments on the manuscript.

Competing interests

The authors declare that they have no competing financial interests.

Correspondence and requests for materials

Correspondence and requests for materials should be addressed to A.H. (email: hamaker@nscl.msu.edu).